Looping metal-support interaction in heterogeneous catalysts during redox reactions

Yue Pan[1,2,7], Shiyu Zhen[3,7], Xiaozhi Liu[1,7], Mengshu Ge[1], Jianxiong Zhao[1], Lin Gu[4], Dan Zhou[5,6]✉, Liang Zhang[3]✉ & Dong Su[1,2]✉

Metal-support interfaces fundamentally govern the catalytic performance of heterogeneous systems through complex interactions. Here, utilizing operando transmission electron microscopy, we uncover a looping metal-support interaction in NiFe-Fe$_3$O$_4$ catalysts during the hydrogen oxidation reaction. At the NiFe-Fe$_3$O$_4$ interfaces, lattice oxygens react with NiFe-activated H atoms, gradually sacrificing themselves and resulting in dynamically migrating interfaces. Meanwhile, reduced iron atoms migrate to the {111} surface of Fe$_3$O$_4$ support and react with oxygen molecules. Consequently, the hydrogen oxidation reaction separates spatially on a single nanoparticle and is intrinsically coupled with the redox reaction of the Fe$_3$O$_4$ support through the dynamic migration of metal-support interfaces. Our work provides previously unidentified mechanistic insight into metal-support interactions and underscores the transformative potential of operando methodologies for studying atomic-scale dynamics.

Heterogeneous catalysts play a pivotal role in a variety of chemical processes, spanning chemical synthesis, energy conversion, and environmental remediation[1-5]. In metal-oxide support systems, oxide serves multiple critical functions: stabilizing metal particles under extreme conditions and modulating catalytic behaviors through metal-support interactions (MSIs)[6-9]. These interactions, primarily governed by the metal-metal or metal-oxygen interactions at the interface[10], can result in complex phenomena such as electronic metal-support interaction (EMSI), strong metal-support interaction (SMSI), and reactive metal-support interaction (RMSI)[11-14]. Such MSIs profoundly influence catalytic performance, directly impacting critical parameters like reaction activity, selectivity, and stability across diverse reactions, including hydrocarbon dehydrogenation, Fischer-Tropsch synthesis, catalytic oxidation, gas/liquid phase reforming, and selective hydrogenation[15-18]. Therefore, understanding interfacial structures and gaining precise control over MSIs has become an important perspective for optimizing catalytic performances[19,20].

Recent advancements in environmental transmission electron microscopy (ETEM) technologies enable real-time observation of catalyst structural evolutions during reactions, providing atomic-scale insights into reaction mechanisms[18,21,22]. These studies have revealed the highly dynamic nature of catalyst structures, which are significantly influenced by the surrounding chemical environment[11,23-26]. In-situ ETEM investigations of Pt-TiO$_2$ systems have revealed remarkable gas-induced oscillations at the metal-support interface, including dramatic structural collapses and reconstructions under redox conditions[21,27]. These transformations are believed to originate from the cyclic generation and refilling of oxygen vacancies. However, despite these results, the fundamental dynamics of MSIs and how their interfacial structure governs catalytic reactions remain poorly understood across many important catalytic systems.

[1]Beijing National Laboratory for Condensed Matter Physics, Institute of Physics, Chinese Academy of Sciences, Beijing, China. [2]University of Chinese Academy of Sciences, Beijing, China. [3]Center for Combustion Energy, School of Vehicle and Mobility, Tsinghua University, Beijing, China. [4]Beijing National Center for Electron Microscopy and Laboratory of Advanced Materials, School of Materials Science and Engineering, Tsinghua University, Beijing, China. [5]DENSsolutions B.V., Delft, the Netherlands. [6]Present address: Leibniz Institute for Crystal Growth, Berlin, Germany. [7]These authors contributed equally: Yue Pan, Shiyu Zhen, Xiaozhi Liu. ✉e-mail: dan.zhou@ikz-berlin.de; zhangbright@tsinghua.edu.cn; dongsu@iphy.ac.cn

In this work, we investigate the reaction dynamics of the NiFe-Fe_3O_4 catalyst during hydrogen oxidation ($H_2 + O_2 \rightarrow H_2O$)[24,27] using the ETEM technique and uncover a novel looping metal-support interaction (LMSI). Yielding only water as the product in gas-phase reactions, the hydrogen oxidation reaction serves as a critical model system for investigating fundamental processes such as adsorption and surface reactions on heterogeneous catalysts[28–30]. Moreover, the coexistence of hydrogen and oxygen simulates redox environments relevant to various catalytic reactions, including CO_2 hydrogenation, CO oxidation, methane combustion, and the water-gas shift reaction, particularly for transition metal catalysts like Ni and Fe, which are readily oxidized and reduced under redox conditions[31–34]. To construct the active interface, we reduce $NiFe_2O_4$ (NFO) with hydrogen, thereby forming a NiFe-Fe_3O_4 structure that enables us to probe the role of Ni in the redox behavior of Fe, as well as to investigate the metal-support interaction under redox conditions.

By controlling the redox environment through gas composition and temperature, we directly visualize reaction-induced solid-solid interfacial migration under reaction conditions and reveal the following mechanism: hydrogen spillover on NiFe nanoparticles provides H^+ to the NiFe-Fe_3O_4 interface, triggering the reduction of Fe_3O_4. Reduced Fe^0 adatoms then migrate substantial distances to the edge sites of Fe_3O_4 {111} planes, where they facilitate oxygen molecule activation. In this process, the redox of iron is coupled with hydrogen oxidation under the catalytic effect of the NiFe nanoparticle. Through quantitative analyses and theoretical calculations, we establish a direct correlation between metal-support interfacial dynamics and catalytic activity. This work highlights the role of LMSI in enhancing catalytic performance and provides novel insights into the fundamental processes of heterogeneous catalysis.

Results

Looping metal–support interaction

As illustrated in Supplementary Fig. 1, we investigate the MSI of NiFe-Fe_3O_4 catalysts using a gas-celled ETEM equipped with a quadrupole mass spectrometer (MS). The NiFe-Fe_3O_4 catalyst is synthesized through the partial reduction of the NFO precursor (Supplementary Figs. 2 and 3). Following a reduction procedure in 10% H_2/He at 400 °C, the NFO nanoparticles transform into a composition of NiFe and Fe_3O_4, as confirmed by selected area electron diffraction (SAED) analysis in Supplementary Fig. 4. The structural characterization of the synthesized NiFe-Fe_3O_4, presented in Supplementary Fig. 5, reveals a classical SMSI state, with NiFe nanoparticles encapsulated by FeO_x layers. Notably, these encapsulated layers exhibit remarkable instability in redox environments, completely retracting from the NiFe nanoparticles upon introduction of the reactant gas mixture (2% O_2, 20% H_2, and 78% He) into the gas cell (Supplementary Fig. 6). This gas-induced destabilization of the encapsulating layers is analogous to behaviors observed in other metal-reducible oxide support systems, where oxygen abstraction from the overlayer under redox conditions leads to dynamic metal-support interactions[27,35–37].

When the reaction temperature exceeds 500 °C, a distinctive catalytic dynamic behavior emerges, characterized by the coordinated migration of NiFe nanoparticles across the Fe_3O_4 support, accompanied by the etching and reconstruction of the support material (Supplementary Movie 1). In contrast, in-situ experiments on pure Ni and Fe_3O_4 catalysts during hydrogen oxidation reaction reveal no comparable dynamic behavior (Supplementary Fig. 7). This dynamic behavior is consistently observed across all NiFe nanoparticles in the NiFe-Fe_3O_4 system, suggesting a significant synergetic interaction between the NiFe nanoparticles and the Fe_3O_4 support, which dynamically responds to the redox reaction environment. We propose a looping metal-support interaction (LMSI) mechanism to describe this phenomenon. The LMSI is primarily driven by high-pressure, high-temperature conditions typical of work conditions, which simulate the

chemical potential of H_2 and O_2 required to promote the structural evolution of the catalysts. These reaction conditions, and the associated structural dynamics they provoke, highlight the critical importance of studying catalyst behavior under authentic operational conditions through real-time operando TEM observations.

Interface dynamics coupled with dual-site redox cycles

HRTEM sequence images captured at 700 °C depict the interface reactions associated with LMSI, as shown in Supplementary Movie 2 and Fig. 1a–f. The images reveal a preferential epitaxial relationship between NiFe nanoparticles and Fe_3O_4 support during the dynamic process. Based on the FFT analysis in Fig. 1g and the simulated SAED pattern in Supplementary Fig. 8, the orientational relationship between the NiFe and Fe_3O_4 particles is determined to be: NiFe ($1\bar{1}2$) // Fe_3O_4 ($1\bar{1}\bar{1}$) and NiFe [110] // Fe_3O_4 [110]. This correlation is further validated by simulating the HRTEM image of the interface structure, which aligns closely with experimental results (Fig. 1h, Supplementary Figs. 9 and 10). Interestingly, the lattice spacing of NiFe ($\bar{1}11$) is 0.20 nm, approximately 15% larger than that of Fe_3O_4 ($2\bar{2}4$) (0.17 nm). This lattice mismatch results in a 4.2° tilting of the NiFe ($1\bar{1}2$) plane relative to the Fe_3O_4 ($1\bar{1}\bar{1}$) plane, a configuration that minimizes interfacial strain[38–40]. Consequently, this tilting leads to the formation of lattice voids along the interface, as illustrated in the structural model presented in Supplementary Fig. 11.

The epitaxial NiFe-Fe_3O_4 interface initially forms a ledge-and-terrace configuration as denoted by the black dashed line in Fig. 1a. Subsequently, the interface migrates through lateral propagation of atomic ledge along the NiFe-Fe_3O_4 interface (Fig. 1b–f). The interface migration process led to the layer-by-layer dissolution of the Fe_3O_4 along the (111) plane, preserving the continuity of the interface structure. The dissolution resembles the Mars-van Krevelen mechanism, where activated hydrogen from NiFe spills over to the interface, facilitating the release of lattice oxygen and reduction of Fe_3O_4[41,42]. During this process, surface Ni (Fe) atoms migrate to lattice voids placed at the interface, driving the migration of NiFe toward the Fe_3O_4 side (Supplementary Fig. 12). Therefore, the vacancies generated by the exsolution of Fe and O from the Fe_3O_4 support are promptly replenished by migrating NiFe atoms, resulting in a self-regulated dynamic interface that minimizes the accumulation of persistent defects. As surface atoms diffuse, the morphology of NiFe deforms with the propagation of NiFe-Fe_3O_4 interface, as illustrated in Supplementary Fig. 13. Although Wulff construction predicts that NiFe nanoparticles would expose {111}, {100}, {311}, {110} surfaces[43], surface-diffusion-induced dynamics result in varying proportions of surface terminations. The metal nanoparticle morphology, induced by interface dynamics, enables NiFe to continuously expose high-index active sites for hydrogen activation. Notably, as the NiFe particle adjusts to achieve lattice matching, its shape changes like a liquid droplet while maintaining its single-crystalline structure[44].

With lattice oxygen released from Fe_3O_4 at the interface, $Fe^{2/3+}$ ions are reduced to mobilizable adatoms that can migrate across the Fe_3O_4 surface, capturing and activating oxygen gas molecules. The activation of oxygen gas takes place at the Fe_3O_4 {111} facets, away from the NiFe-Fe_3O_4 interface, as illustrated in Supplementary Movie 3. As shown in Fig. 1i, the Fe_3O_4 predominantly exposes the atomically flat {111} facets. Upon reaction between reduced Fe adatoms and oxygen gas molecules, a monoatomic layer nucleates at the flat {111} plane of the Fe_3O_4, creating a step-terrace configuration, as marked by the red arrows in Fig. 1j. This newly formed atomic layer then grows laterally through step-flow growth with Fe and O adatoms attaching to the step edge (Fig. 1k–n). The Fe atoms, originating from the NiFe-Fe_3O_4 interface and diffusing outward on the Fe_3O_4 support, facilitate the dissociative adsorption of O_2 molecules[23]. The growth behavior ensures that the Fe_3O_4 support continuously exposes {111} planes, lowering the system's energy. Overall, the LMSI of NiFe-Fe_3O_4 catalysts
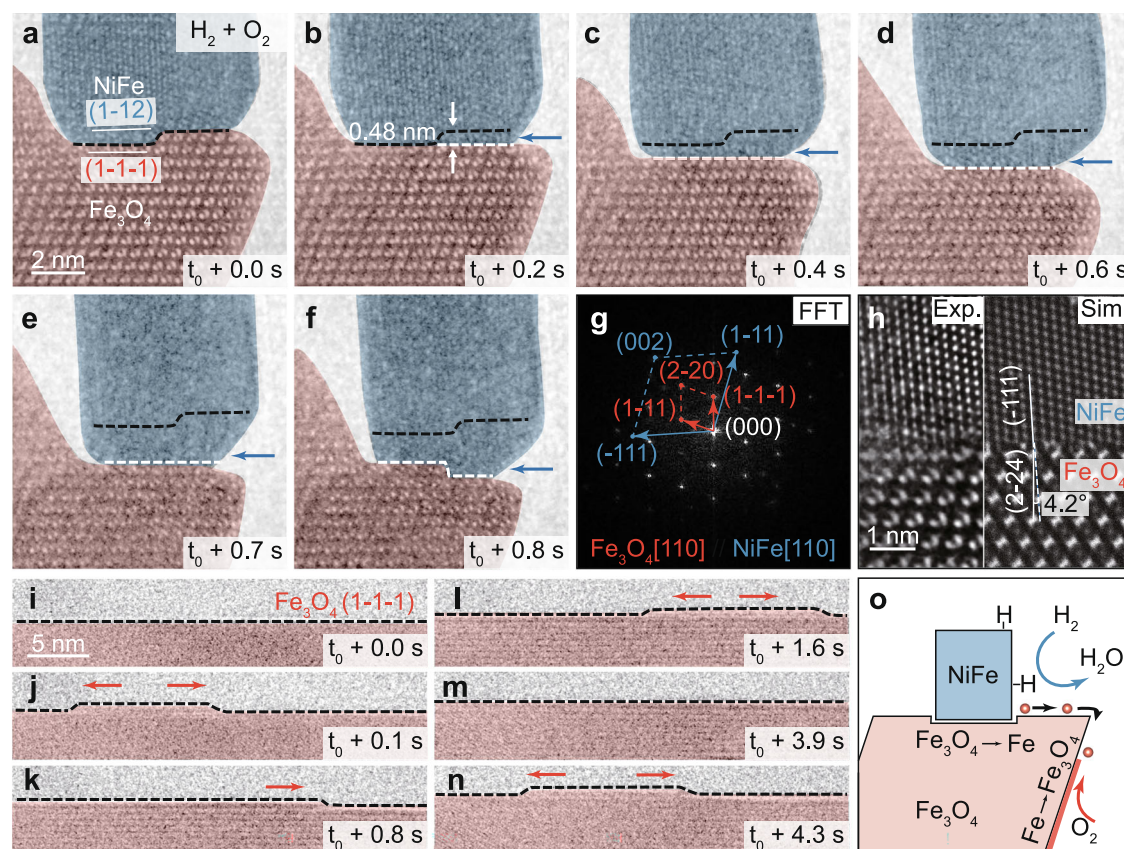
Fig. 1 | Atomic-resolution observation of the LMSI of NiFe-Fe$_3$O$_4$ catalyst.
a–**f** Time-sequence HRTEM images of a NiFe-Fe$_3$O$_4$ nanoparticle under hydrogen oxidation reaction at 700 °C from Supplementary Movie 2, showing surface-diffusion-induced migration of the NiFe nanoparticle, along with the layer-by-layer reduction of Fe$_3$O$_4$. **g** FFT pattern of **a** illustrating the epitaxial relationship between the NiFe and Fe$_3$O$_4$, i.e., NiFe (1$\bar{1}$2) // Fe$_3$O$_4$ (1$\bar{1}\bar{1}$) and NiFe [110] // Fe$_3$O$_4$ [110]. **h** is an enlarged image of a selected region in (**a**). In comparison, a simulated HRTEM image is also shown. **i**–**n** Observed layer-by-layer growth of Fe$_3$O$_4$ at the surface of Fe$_3$O$_4$ from Supplementary Movie 3. **o** Schematic image illustrates the relation between the LMSI effect and catalytic reactions. The reduction of Fe$_3$O$_4$ at the NiFe-Fe$_3$O$_4$ interface resulted in the migration of the interface. Additionally, the oxidation of Fe at the edge sites of the Fe$_3$O$_4$ {111} planes leads to the growth of Fe$_3$O$_4$.

align with gas-solid reactions at separated sites, including the reduction of Fe$_3$O$_4$ at NiFe-Fe$_3$O$_4$ interface and oxidation of Fe adatoms at Fe$_3$O$_4$ {111} sites, as illustrated in Fig. 1o. These two gas-solid reactions are synergistically facilitated by the migration of Fe adatoms.

TEM images (Supplementary Fig. 14) and the movie (Supplementary Movie 1) recorded at 700 °C reveal that the LMSI between NiFe and Fe$_3$O$_4$ significantly contributes to its structural dynamics. The simultaneous reduction and oxidation of Fe$_3$O$_4$ are governed by the chemical potential of the gas phase, which drives the system into a nonequilibrium dynamic state[23,24,45,46]. As shown in Supplementary Fig. 15, we investigate the NiFe-Fe$_3$O$_4$ catalysts under varying H$_2$/O$_2$ ratios and find that increasing the oxygen content suppresses redox dynamics, necessitating higher temperatures to initiate interface reduction and surface oxidation processes.

Time-sequence TEM images of a NiFe-Fe$_3$O$_4$ system in Fig. 2a to h and Supplementary Movie 4 illustrate the synergistic effect between interfacial reduction and surface oxidation of Fe$_3$O$_4$. The phases of NiFe and Fe$_3$O$_4$ are confirmed by the corresponding filtered inverse Fast Fourier Transform (iFFT) presented in Fig. 2i. To clearly illustrate interface migration and surface growth, the NiFe nanoparticle and growth Fe$_3$O$_4$ layers are denoted by blue and red colors, respectively. It is evident that as the interface migrates, the Fe$_3$O$_4$ support is etched, exposing a pathway, while simultaneously, Fe$_3$O$_4$ layers grow at the {111} planes near the interface. In Fig. 2j, we track the trajectory of the NiFe nanoparticle, revealing its movement along the <112> direction of Fe$_3$O$_4$. This directional movement correlates with layer-by-layer

etching of the Fe$_3$O$_4$ at {111} planes. Additionally, the etching process exposes new {111} planes of Fe$_3$O$_4$ along the path of the NiFe nanoparticle. Upon reaching the boundary of the Fe$_3$O$_4$, the NiFe nanoparticle reorients and continues its movement in the specific direction (Fig. 2e–f, Supplementary Figs. 13 and 16). The directional migration of NiFe nanoparticles, along with the specific lattice growth of Fe$_3$O$_4$, ensures that the Fe$_3$O$_4$ consistently exposes low-index {111} planes, thereby minimizing the total energy of the catalyst system[47,48]. We have recorded the movement of different nanoparticles (Supplementary Fig. 17), confirming the above-mentioned conclusions. We find that the reduction and oxidation processes are coupled, forming an integral part of the overall hydrogen oxidation reaction. Although reduction and oxidation occur at separate sites, the proportions of Fe$_3$O$_4$ and NiFe remain steady, as evidenced by the measured projection area in Fig. 2k, further confirming the coupled iron redox process.

To further clarify the correlation between the LMSI and catalytic activity, we simultaneously measured the MS signals of oxygen and water in Fig. 3a. The results reveal the production of H$_2$O and the consumption of O$_2$ at temperatures above 500 °C, suggesting that the hydrogen oxidation reaction occurs. In contrast, blank experiments using empty chips (Supplementary Fig. 18) show no variation in signal with temperature increases up to 900 °C, confirming that the detected water signal originates from catalytic H$_2$-O$_2$ reaction. Additionally, sole Fe$_3$O$_4$ nanoparticles exhibit no catalytic activity nor LMSI effect under the same conditions (Supplementary Figs. 7 and 19). In-situ SAED pattern recorded during the structural dynamics (Fig. 3b) and
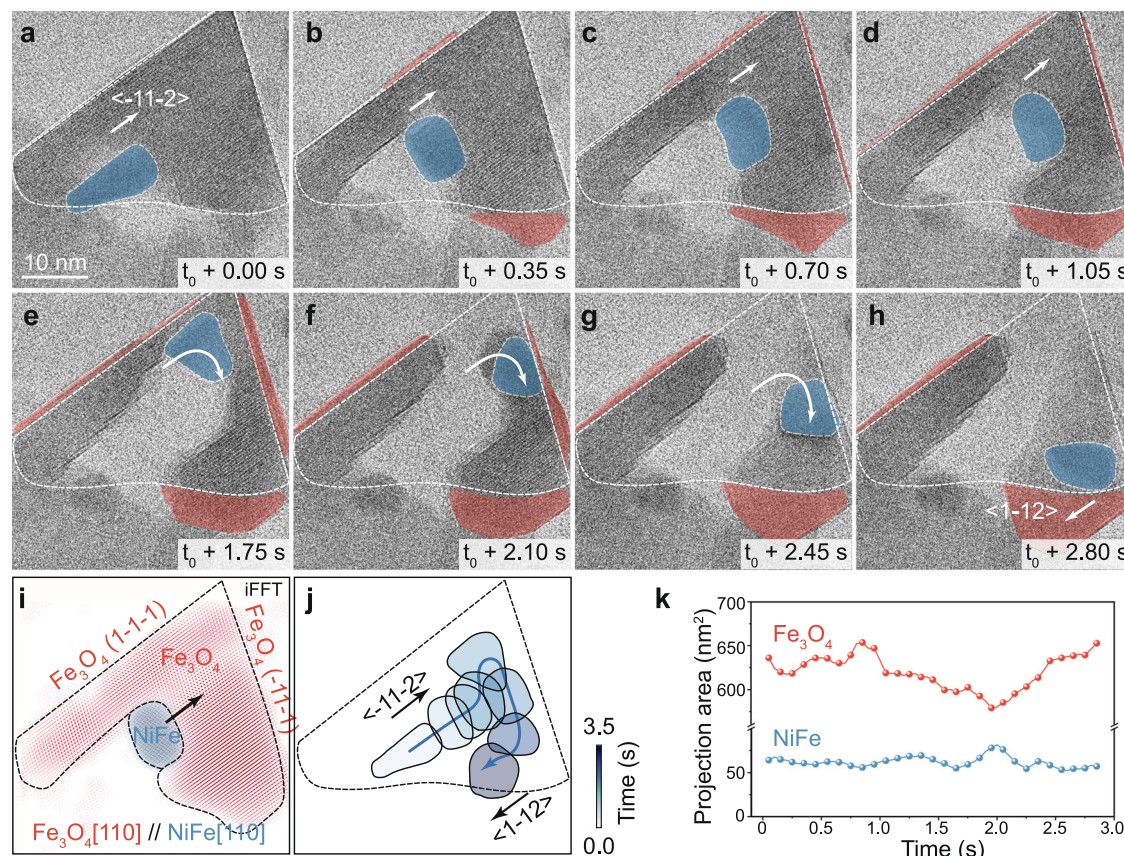
Fig. 2 | Dynamic LMSI in NiFe-Fe$_3$O$_4$ catalysts during hydrogen oxidation reaction. a–h Time-sequence HRTEM images of NiFe-Fe$_3$O$_4$ catalyst at 700 °C at an O$_2$/H$_2$ ratio of 1/10 in Supplementary Movie 4. **i** Filtered inverse FFT of HRTEM image in **b** shows the correlated orientation between Fe$_3$O$_4$ and NiFe. **j** Trace of motion path and morphology evolution of the NiFe nanoparticle in Supplementary Movie 4. **k** Projection area of Fe$_3$O$_4$ and NiFe in function of time from Supplementary Movie 4.

corresponding peaks analysis (Fig. 3c) suggest that the observed structural dynamics arise from phase transitions between NiFe and Fe$_3$O$_4$. We simultaneously record the structural evolution of the NiFe-Fe$_3$O$_4$ catalyst during the above reaction process, as illustrated in Fig. 3d–h and Supplementary Movies 5–9. At the onset of the reaction at 500 °C, LMSI effects in the NiFe-Fe$_3$O$_4$ nanoparticles are observed (Supplementary Figs. 20 and 21). As the temperature increases to 600 °C, water production rises significantly, accompanied by more pronounced LMSI effects of the nanoparticles (Supplementary Movie 7). The enhanced structural dynamics are also accompanied by an increase in NiFe particle size by both Ostwald ripening and coalescence process (Supplementary Fig. 22). However, the growth becomes limited as the temperature exceeds 700 °C, suggesting that particle sintering is constrained by dynamic interface interactions.

Mechanistic insights from quantification and computations
To quantify these dynamics, we have employed an optical flow method to quantitatively track the movement velocity of nanoparticles[49]. As shown in Fig. 3i–m, the velocity of particle movement increases notably from 400 °C to 600 °C, reflecting a consistent trend with catalytic activity. With the reaction temperature reaching 800 °C, both MS signals and the velocity of particle movement reach a steady state. In-situ SAED patterns are also recorded from 400 °C to 800 °C (heat rate: 1 °C/s) to illustrate the structural dynamics above 500 °C (Supplementary Movie 10). A diffraction-spot-detection method[50] is employed to track these dynamic diffraction spots (Supplementary Movie 11), revealing a noticeable reduction in their lifespan (Fig. 3n). Our statistics analysis of the average velocity magnitudes of the structural dynamics and the average lifespan of the dynamic

diffraction spots (Fig. 3o) further corroborates the close relationship between LMSI and catalytic activity.

We investigate the LMSI effect on the spatially decoupled hydrogen oxidation reaction in the NiFe-Fe$_3$O$_4$ system through DFT calculations with Hubbard U correction, as shown in Fig. 4a. The computed Gibbs free energy diagram reveals an exceptionally low hydrogen dissociation barrier of 0.11 eV for the NiFe-Fe$_3$O$_4$ system, which is significantly lower than the barriers observed for Fe$_3$O$_4$ and Fe-Fe$_3$O$_4$ systems (Supplementary Fig. 23). The activated hydrogen then spillover to the interface, promoting the reduction of the Fe$_3$O$_4$ support, as discussed in detail by Prins, R[51]. NN-MD simulations further elucidate the interface reduction mechanism, demonstrating that NiFe preferentially attracts oxygen from the Fe$_3$O$_4$ due to its stronger oxygen affinity compared to Fe-Fe$_3$O$_4$ (Fig. 4b, c, and Supplementary Fig. 24–26). This phenomenon, termed the oxygen reverse spillover effect, facilitates the reduction of Fe$_3$O$_4$ layers at the interface[52] (Supplementary Note 3). This observed tendency of oxygen attraction to NiFe aligns closely with our experimental findings from reduction and oxidation experiments on the NFO sample (Supplementary Notes 4 and 5). The attracted oxygen atoms on the NiFe surface are subsequently reduced by dissociated hydrogen atoms, forming water through a process that is substantially more efficient than on pure Fe, where hydrogen activation and water formation typically constitute rate-limiting steps (Supplementary Figs. 27–29).

Concurrently, the reduced Fe atoms migrate to the Fe$_3$O$_4$ {111} facets, where they undergo re-oxidization by oxygen. This migration proceeds significantly more rapidly on the surface than through the Fe$_3$O$_4$ bulk (Fig. 4d). Besides, the NiFe's superior H$_2$ dissociation activity enables hydrogen spillover across a broader region on the
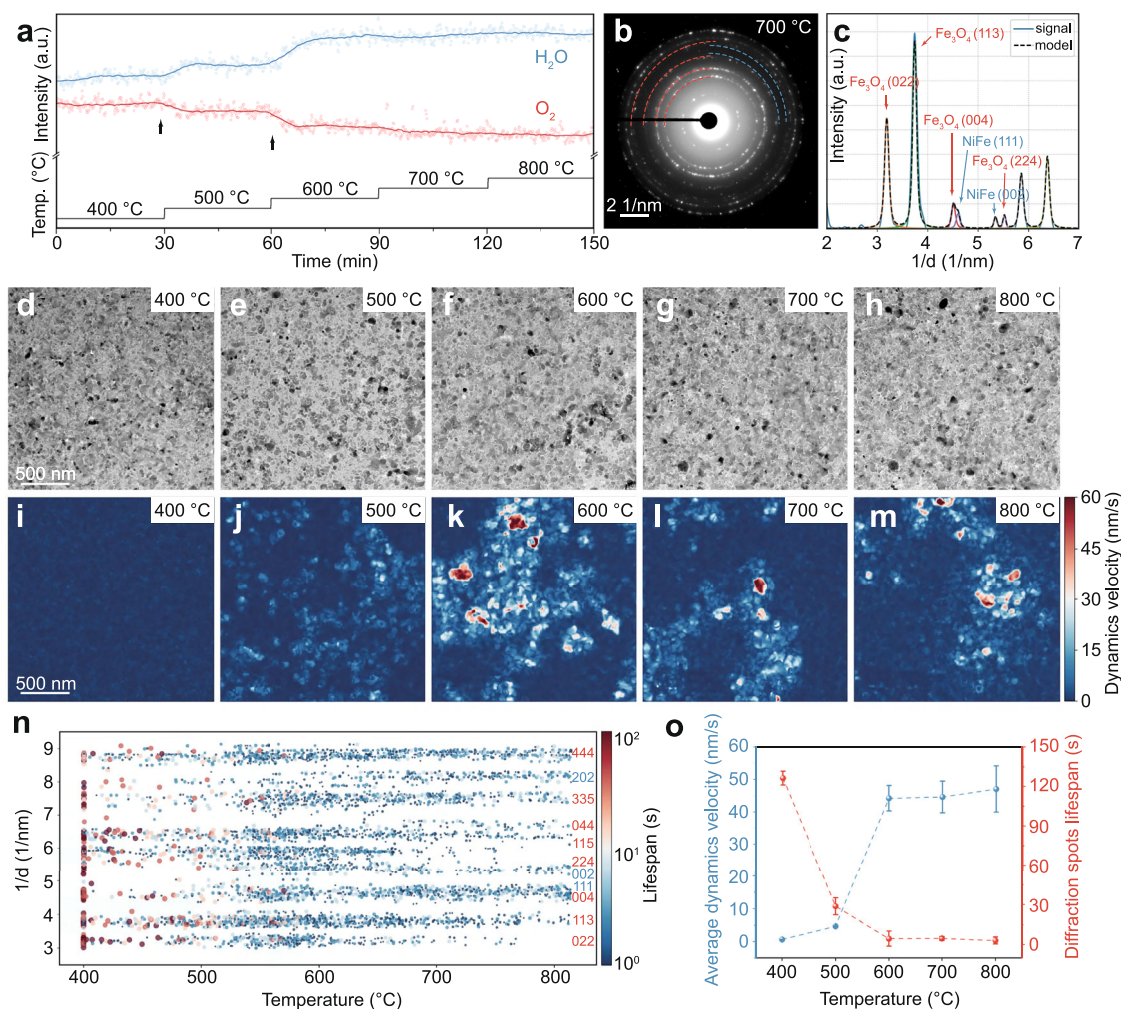
Fig. 3 | Correlation between the LMSI and catalytic activity of NiFe-Fe₃O₄ catalyst in hydrogen oxidation reaction. a Operando MS data obtained post-TEM at temperatures from 400 °C to 800 °C. **b, c** SAED pattern and corresponding peaks analysis of the catalyst. **d−h** Representative TEM images of NiFe-Fe₃O₄ nanoparticles at different temperatures captured from Supplementary Movie 5−9. **i−m** Dynamics velocity analyses with an optical flow method based on Supplementary Movie 5−9. **n** Lifespan from tracking diffraction spots of in-situ SAED (Supplementary Movies 10 and 11) pattern captured with heating under ambient conditions. The reciprocal spacing and lifespan of each dot are shown in the function of temperature. **o** The average dynamics velocity (blue dots), and the lifespan of diffraction spots (red dots) across various temperature stages illustrate a close correlation between structural dynamics and catalytic activity.

NiFe-Fe₃O₄ system, creating an extended hydrogen-rich environment. As a result, Fe atoms in the NiFe-Fe₃O₄ system need to traverse a longer distance before re-oxidation compared to those in the Fe-Fe₃O₄ system. This extended Fe diffusion pathway is fundamental to the spatially decoupled redox process characteristic of NiFe-Fe₃O₄, which distinguishes it from the more localized redox behavior seen in Fe-Fe₃O₄. The energy profile illustrating the dissociation pathway of molecular oxygen (O_2) on an Fe adatom anchored to the Fe₃O₄ surface (Supplementary Fig. 30) shows that the energy barrier is low, indicating that this step is not rate-limiting in the redox cycle. Figure 4e provides a comprehensive visualization of the correlation between LMSI and the hydrogen oxidation mechanism in NiFe-Fe₃O₄. The dynamic process is characterized by spatially decoupled hydrogen and oxygen activation (hydrogen activation occurs around NiFe, while oxygen activation takes place at distant Fe₃O₄ {111} facets). This is accompanied by Fe₃O₄ reduction, Fe atom migration, and subsequent re-oxidation. The low H_2 dissociation barrier on NiFe, combined with rapid surface diffusion of Fe atoms, facilitates efficient hydrogen spillover and swift Fe atom migration. These factors are crucial in enabling spatial separation that defines the unique LMSI phenomenon in the NiFe-Fe₃O₄ system.

In summary, our comprehensive investigation using operando ETEM reveals a new type of metal-support interaction in the NiFe-Fe₃O₄ catalyst system. The $Fe^{2/3+}/Fe^0$ redox cycles demonstrate remarkable spatial segregation, activating hydrogen and oxygen at distinctly different locations. This mechanism drives two critical processes: reduction (etching) of Fe₃O₄ at the NiFe-Fe₃O₄ interface and promoting growth of Fe₃O₄ layers along the {111} planes. The LMSI effect emerges from the inherent reducibility of the Fe₃O₄ support, with interface migration precisely orchestrated by the movement of reduced iron species. NiFe nanoparticles play a role in prompting the spillover of hydrogen and accelerating the iron redox process. By elucidating the intricate interplay between catalyst components, we establish a fundamental correlation between the LMSI effect and catalytic performance. Beyond this specific case, we suggest a broader applicability of LMSI to heterogeneous catalytic systems containing transition metal-oxide support. The hydrogen spillover can occur on metallic nanoparticles, coupling with the redox circles of other types of transition metal-oxide support, consequently enhancing overall catalytic reactivity. By unveiling the sophisticated spatial and chemical dynamics at the catalyst interface, our research provides a transformative
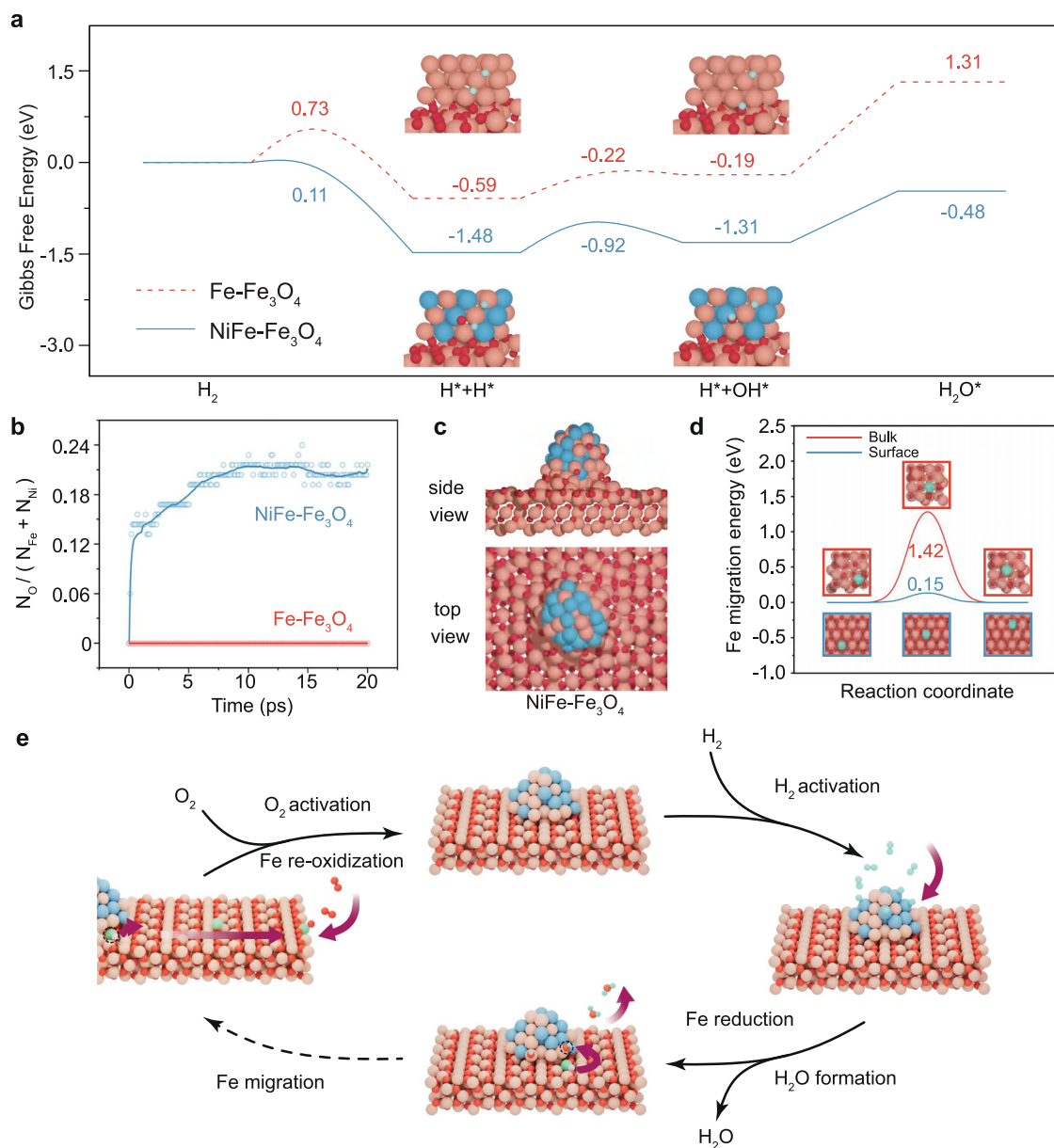
Fig. 4 | Theoretical analysis of the atomic reaction pathway on the NiFe-Fe₃O₄ catalyst. a DFT calculated Gibbs free energy diagram for the hydrogen oxidation reaction on NiFe-Fe₃O₄ (blue solid), and Fe-Fe₃O₄ (red dashed). Insets show optimized structures of intermediate states. Cyan, pink, red, and pale turquoise balls display Ni, Fe, O, and H atoms, respectively. **b** Amount of accumulated oxygen atoms on NiFe and Fe nanoparticles from NN-MD simulations, showing that NiFe facilitates the migration of lattice oxygen from the Fe₃O₄ to the NiFe nanoparticle. **c** Side and top view of NiFe-Fe₃O₄ after 20 ps NN-MD simulation. **d** Energy profile for activated Fe atom transfer on Fe₃O₄. **e** Schematics representation of the mechanisms underlying the LMSI effect in hydrogen oxidation on the NiFe-Fe₃O₄ catalyst.

perspective on metal-support interactions, potentially guiding the design of highly efficient heterogeneous catalysts.

Methods

Operando TEM setup

The operando TEM experiments were conducted using a JEM-F200, a DENSsolutions Climate G+ gas supply system, and a quadrupole mass spectrometer (Supplementary Fig. 1). It has been shown that the purity of the gas composition significantly affects the state of nanoparticles, and optimizing the environment in ETEM can closely simulate actual working conditions. To prevent contamination of pipelines, we construct our gas supply system using stainless steel or poly(ether-ether-ketone)−silica, minimizing leakage and moisture adsorption. Gas filters tailored for different gas sources (including hydrogen, oxygen, and

helium) are also implemented to remove various impurities, such as oxygen, moisture, and hydrocarbon contaminants. Additionally, a complete workflow for operando experiments is proposed, including leakage testing and pipeline flushing, to ensure precise control of the microenvironment in the gas-cell nanoreactor.

After completing the preparation procedures, NFO samples are dispersed in ethanol with sonication, then drop-cast onto a micro-electromechanical system (MEMS)-based heating chip. This heating chip is sealed with another chip featuring a large electron-transparent Si₃N₄ membrane for imaging, forming a nanoreactor capable of encapsulating gas at pressure up to 1 bar, allowing the investigation of structural evolution under working conditions. To enable atomic-scale observation of nanoparticle structural dynamics, a new type of chip featuring thinner membranes (30 nm) is employed. The nanoreactor is

then assembled into the TEM holder and inserted into the TEM chamber. The oxide nanoparticles are initially heated to 400 °C in 10% O_2/He to remove contamination. To create a hydrogen oxidation environment, a mixture of 2% O_2/20% H_2/He (4% O_2/20% H_2/He, and 10% O_2/20% H_2/He) is introduced into the nanoreactor, with mass spectrum data collected using the gas released from the nanoreactor. To minimize the influence of water produced during the reaction on structural evolution, we employ a high gas flow rate (0.2 mln/min) to efficiently remove water from the reaction zone.

Sample preparation
$NiFe_2O_4$ nanoparticles (≥99.5%) used for operando TEM experiments were purchased from Alfa Aesar, and the TEM characterization results are shown in Supplementary Figs. 2 and 3. $NiFe_2O_4$ has an inverse spinel structure similar to Fe_3O_4, with half of the trivalent ions (Fe^{3+}) occupying tetrahedral sites, while divalent ions (Ni^{2+}, Fe^{2+}), and the remaining trivalent iron ions (Fe^{3+}) occupy octahedral sites[53]. Upon heating in hydrogen, $NiFe_2O_4$ is reduced to $NiFe-Fe_3O_4$, which can be used to catalyze the hydrogen oxidation reaction.

TEM characterization
TEM images and movie series are recorded by a Gatan Rio camera at a 2048×2048 pixel resolution under an exposure time of 0.05 s. The elemental composition, as well as distribution, are studied on the microscope equipped with an energy-dispersive X-ray analyzer. Electron energy loss spectroscopy (EELS) is collected with a Gatan Imaging Filter (GIF) Quantum Model 1077 spectrometer.

Dynamic analysis based on the optical flow field
To quantitatively analyze the LMSI within the in-situ data, we compute the mean displacement vector to measure the extent of the changes between successive frames. The Farnebäck Dense Optical Flow algorithm[49] is utilized to establish the motion field for individual frames. Given our emphasis on the scale of change, the angles of the motion vectors are not considered in this investigation. Consequently, the magnitudes of these motion vectors are leveraged to assess the degree of motion (Fig. 3i–m). The magnitudes of the motion vectors of the NiFe catalysts exhibit similar trends of change as the catalytic activity (Fig. 3a).

In-situ SAED spots tracking
We apply automatic center identification on in-situ SAED data (Supplementary Movie 10) using the MS-Trans model[54]. The diffraction spots are detected utilizing a Laplacian of Gaussian blob detection algorithm (Supplementary Movie 11). The elliptical distortion is measured on the first frame using peak finding and an ellipse fitting algorithm as mentioned in ref. 50. The resulting fitted maximum and minimum semi-axes are 422.5 pixels and 421.5 pixels, respectively. The one-pixel discrepancy is likely due to the quantification effects. Therefore, elliptical distortion is neglected in the data processing stage. We monitor the diffraction spots, recording the time each spot appears and disappears to calculate its lifespan. In Fig. 3n, we plot the diffraction spots as a function of temperature (x-axis) and reciprocal spacing (y-axis). These spots are indexed to either the Fe_3O_4 phase or the NiFe phase, with corresponding crystal planes labeled on the right side of Fig. 3n. The spots' different colors and sizes indicate their respective lifespans. As the nanoreactor is raised to reaction temperature, a noticeable decrease in the lifespan of diffraction spots highlights the reaction-related structure dynamics. We select the Fe_3O_4 (113) diffraction spots to calculate the average lifespan and assess the structural dynamics of the $NiFe-Fe_3O_4$ catalyst (Fig. 3o).

Density functional theory (DFT)
The spin-polarized calculations with the projector-augmented wave (PAW) method are performed based Vienna Ab Initio Simulation package (VASP 5.4.4)[55]. The exchange and correlation effects are described by the Perdew–Burke–Ernzerhof functional (PBE)[55,56]. The DFT + U method is used to accurately simulate electron strong correlation in the transition-metal oxide systems[57]. The Hubbard parameters (U) are introduced for the Fe_3d and Ni_3d electrons with the Ueff (= U - J) values of 3.80 eV and 5.77 eV according to previous theoretical work[58,59]. The optimization calculations are employed with a cutoff energy of 400 eV and an atomic force convergence of 0.02 eV/Å. To accurately characterize the magnetic properties of this system, we systematically reference the theoretical studies by Jiao and Wen et al. on Fe_3O_4 to appropriately set the spin of octahedral and tetrahedral Fe[60,61]. Among the six possible terminations of the Fe_3O_4 (111) surface, the Fe_{oct2}-terminated surface is the most stable as hypothesized by STM experiments[62] as well as previous theoretical studies[63]. Therefore, we choose the Fe_{oct2}-terminated surface as the model for our studies. For the (111)-Fe_{oct2} model, a p (1×1) supercell slab model with 4 atomic-layer thickness is selected. In order to save computer time, 2 atomic layers at the bottom are fixed to simulate the bulk phase, and the top 2 atomic layers are allowed to relax. We apply Monkhorst-Packmesh k points of $(3 \times 3 \times 1)$ for this surface. For $NiFe-Fe_3O_4$ and $Fe-Fe_3O_4$ models, we use a four-layer p (2×2) model with a supported NiFe/Fe nanorod, referencing the modeling of interfaces in previous work by Chandler et al.[64]. Because of the relatively large cell size, the sampling of the Brillouin zone was restricted to the gamma point. To avoid the interaction between periodic layers, the vacuum layer thickness of both models is 15 Å.

The free energy for the intermediate is calculated as $\Delta G = \Delta E + \Delta ZPE - T\Delta S$, where ΔE is the reaction energy change from DFT calculations, ΔZPE is the change of zero-point energies (ZPE), which is calculated with the vibrational frequencies of adsorbates and molecules, and ΔS is the entropy change in the reaction. T is the reaction temperature. Furthermore, all barrier calculations are performed by using the climbing-image nudged elastic band method (NEB) and further improved by the dimer method[65]. The activation energy is calculated by ($E_{TS} - E_{IS}$), where E_{TS} is the energy of the transition state, and E_{IS} is the energy of the initial state.

Molecular dynamics simulations based on neuron network potential
To provide information on LMSI over a larger time and spatial scale, we perform molecular dynamics simulations using a global stochastic surface walking neural network (NN) potential by a commercial software named LASP developed by Zhipan Liu group (LASP 3.4.5)[66]. We construct a NiFe/Fe nanoparticle of 1.5 nm × 1.5 nm (containing 82 atoms), supported by a 5 nm × 4 nm Fe_3O_4 (111) substrate (containing 720 Fe atoms and 960 O atoms), to investigate the migration of oxygen in a large-scale model, in total 1762 atoms, through theoretical calculations. Molecular dynamics simulations with neural network potential (NN-MD) are performed at a constant temperature ($T = 673$ K) within the NVT ensemble. We conduct a 20 ps simulation of the $NiFe-Fe_3O_4$ system, which demonstrates that NiFe facilitates the migration of lattice oxygen from the Fe_3O_4 to the NiFe nanoparticle. However, in our longer 1000 ps simulation of the Fe system, we observe no migration of lattice oxygen from the Fe_3O_4 substrate to the Fe nanoparticle. In our model, the z-axis coordinates of the top-layer oxygen atoms of Fe_3O_4 are approximately 19.5 Å. Considering the migration effect, we define oxygen atoms with z-axis coordinates greater than 20 Å as oxygen atoms on the nanoparticle, which is consistent with our observations from the MD frames.

Data availability
All data generated in this study are provided in the main text and the Supplementary Information. All data are available upon request from corresponding authors.

References

1. Liu, L. & Corma, A. Metal catalysts for heterogeneous catalysis: from single atoms to nanoclusters and nanoparticles. *Chem. Rev.* **118**, 4981–5079 (2018).
2. Zhao, J.-W. et al. Crystal-phase engineering in heterogeneous catalysis. *Chem. Rev.* **124**, 164–209 (2024).
3. Li, Z. et al. Well-defined materials for heterogeneous catalysis: from nanoparticles to isolated single-atom sites. *Chem. Rev.* **120**, 623–682 (2020).
4. Thomas, J. M. & Thomas, W. J. *Principles and practice of heterogeneous catalysis* (Wiley, 2015).
5. Fujiwara, K., Okuyama, K. & Pratsinis, S. E. Metal–support interactions in catalysts for environmental remediation. *Environ. Sci. Nano* **4**, 2076–2092 (2017).
6. Dai, Y., Lu, P., Cao, Z., Campbell, C. T. & Xia, Y. The physical chemistry and materials science behind sinter-resistant catalysts. *Chem. Soc. Rev.* **47**, 4314–4331 (2018).
7. Divins, N. J., Angurell, I., Escudero, C., Pérez-Dieste, V. & Llorca, J. Influence of the support on surface rearrangements of bimetallic nanoparticles in real catalysts. *Science* **346**, 620–623 (2014).
8. Li, Y., Zhang, Y., Qian, K. & Huang, W. Metal–support interactions in metal/oxide catalysts and oxide–metal interactions in oxide/metal inverse catalysts. *ACS Catal.* **12**, 1268–1287 (2022).
9. Farmer, J. A. & Campbell, C. T. Ceria maintains smaller metal catalyst particles by strong metal-support bonding. *Science* **329**, 933–936 (2010).
10. Wang, T. et al. Nature of metal-support interaction for metal catalysts on oxide supports. *Science* **386**, 915–920 (2024).
11. Tauster, S. J. Strong metal-support interactions. *Acc. Chem. Res.* **20**, 389–394 (1987).
12. Tauster, S. J., Fung, S. C. & Garten, R. L. Strong metal-support interactions. Group 8 noble metals supported on titanium dioxide. *J. Am. Chem. Soc.* **100**, 170–175 (1978).
13. Yang, J., Li, W., Wang, D. & Li, Y. Electronic metal–support interaction of single-atom catalysts and applications in electrocatalysis. *Adv. Mater.* **32**, 2003300 (2020).
14. Penner, S. & Armbrüster, M. Formation of intermetallic compounds by reactive metal–support interaction: a frequently encountered phenomenon in catalysis. *ChemCatChem* **7**, 374–392 (2015).
15. Matsubu, J. C. et al. Adsorbate-mediated strong metal–support interactions in oxide-supported Rh catalysts. *Nat. Chem.* **9**, 120–127 (2017).
16. Lykhach, Y. et al. Counting electrons on supported nanoparticles. *Nat. Mater.* **15**, 284–288 (2016).
17. Zhao, J. et al. Tuning the CO_2 hydrogenation activity via regulating the strong metal-support interactions of the Ni/Sm_2O_3 catalyst. *ACS Catal.* **14**, 3158–3168 (2024).
18. Chen, S. et al. Defective TiO_x overlayers catalyze propane dehydrogenation promoted by base metals. *Science* **385**, 295–300 (2024).
19. van Deelen, T. W., Hernández Mejía, C. & de Jong, K. P. Control of metal-support interactions in heterogeneous catalysts to enhance activity and selectivity. *Nat. Catal.* **2**, 955–970 (2019).
20. Wu, P. et al. Harnessing strong metal–support interactions via a reverse route. *Nat. Commun.* **11**, 3042 (2020).
21. Monai, M. et al. Restructuring of titanium oxide overlayers over nickel nanoparticles during catalysis. *Science* **380**, 644–651 (2023).
22. Plodinec, M. et al. Versatile homebuilt gas feed and analysis system for operando TEM of catalysts at work. *Microsc. Microanal.* **26**, 220–228 (2020).
23. Chen, X. et al. Atomistic origins of reversible noncatalytic gas–solid interfacial reactions. *J. Am. Chem. Soc.* **145**, 3961–3971 (2023).
24. Huang, X. et al. Phase coexistence and structural dynamics of redox metal catalysts revealed by operando TEM. *Adv. Mater.* **33**, 2101772 (2021).
25. Liu, J. Advanced electron microscopy of metal–support interactions in supported metal catalysts. *ChemCatChem* **3**, 934–948 (2011).
26. Shi, X. Y. et al. Real-space observation of strong metal-support interaction: state-of-the-art and what's the next. *J. Microsc.* **262**, 203–215 (2016).
27. Frey, H., Beck, A., Huang, X., van Bokhoven, J. A. & Willinger, M. G. Dynamic interplay between metal nanoparticles and oxide support under redox conditions. *Science* **376**, 982–987 (2022).
28. Schwarzer, M. et al. Cooperative adsorbate binding catalyzes high-temperature hydrogen oxidation on palladium. *Science* **386**, 511–516 (2024).
29. Cao, J. et al. In situ observation of oscillatory redox dynamics of copper. *Nat. Commun.* **11**, 3554 (2020).
30. Suchorski, Y. et al. Visualizing catalyst heterogeneity by a multi-frequential oscillating reaction. *Nat. Commun.* **9**, 600 (2018).
31. Kim, S. M. et al. Cooperativity and dynamics increase the performance of NiFe dry reforming catalysts. *J. Am. Chem. Soc.* **139**, 1937–1949 (2017).
32. Theofanidis, S. A., Galvita, V. V., Poelman, H. & Marin, G. B. Enhanced carbon-resistant dry reforming Fe-Ni catalyst: role of Fe. *ACS Catal.* **5**, 3028–3039 (2015).
33. Zhu, J. et al. Dynamic structural evolution of iron catalysts involving competitive oxidation and carburization during CO_2 hydrogenation. *Sci. Adv.* **8**, eabm3629 (2022).
34. Liu, X. et al. Atomically resolved transition pathways of iron redox. *J. Am. Chem. Soc.* **146**, 17487–17494 (2024).
35. Beck, A. et al. The dynamics of overlayer formation on catalyst nanoparticles and strong metal-support interaction. *Nat. Commun.* **11**, 3220 (2020).
36. Salusso, D. et al. Direct evidence of dynamic metal support interactions in Co/TiO_2 catalysts by near-ambient pressure X-ray photoelectron spectroscopy. *Nanomaterials* **13**, 2672 (2023).
37. Shu, G. et al. Dynamic metal-support interaction-activated sub-nanometer Pt clusters on FeO_x supports for aqueous phase reforming and hydrogenolysis of glycerol. *ACS Catal.* **13**, 8423–8436 (2023).
38. Riesz, F. Rotated tilting in lattice-mismatched heteroepitaxial systems. *J. Cryst. Growth* **140**, 213–218 (1994).
39. LaGrow, A. P., Ward, M. R., Lloyd, D. C., Gai, P. L. & Boyes, E. D. Visualizing the Cu/Cu_2O interface transition in nanoparticles with environmental scanning transmission electron microscopy. *J. Am. Chem. Soc.* **139**, 179–185 (2017).
40. Hirth, J. P. Ledges and dislocations in phase transformations. *Metall. Mater. Trans. A* **25**, 1885–1894 (1994).
41. Bliem, R. et al. An atomic-scale view of CO and H_2 oxidation on a Pt/Fe_3O_4 model catalyst. *Angew. Chem. Int. Ed.* **54**, 13999–14002 (2015).
42. Doudin, N. et al. Understanding heterolytic H_2 cleavage and water-assisted hydrogen spillover on Fe_3O_4(001)-supported single palladium atoms. *ACS Catal.* **9**, 7876–7887 (2019).
43. Liu, J., Su, H., Sun, D., Zhang, B. & Li, W. Crystallographic dependence of CO activation on cobalt catalysts: HCP versus FCC. *J. Am. Chem. Soc.* **135**, 16284–16287 (2013).
44. Sun, J. et al. Liquid-like pseudoelasticity of sub-10-nm crystalline silver particles. *Nat. Mater.* **13**, 1007–1012 (2014).
45. Tang, M. et al. Oscillatory active state of a Pd nanocatalyst identified by in situ capture of the instantaneous structure-activity change at the atomic scale. *J. Am. Chem. Soc.* **146**, 18341–18349 (2024).
46. Yue, S. et al. Redox dynamics and surface structures of an active palladium catalyst during methane oxidation. *Nat. Commun.* **15**, 4678 (2024).
47. Santos-Carballal, D., Roldan, A., Grau-Crespo, R. & de Leeuw, N. H. A DFT study of the structures, stabilities and redox behaviour of the major surfaces of magnetite Fe_3O_4. *Phys. Chem. Chem. Phys.* **16**, 21082–21097 (2014).

48. Cornell, R. M. & Schwertmann, U. *The iron oxides: structure, properties, reactions, occurences and uses* 59-94 (Wiley, 2003).

49. Farnebäck, G. Two-frame motion estimation based on polynomial expansion. *Image analysis*, Lecture Notes in Computer Science, (eds Bigun J. & Gustavsson T.) vol. 2749, 363–370 (Springer, Berlin Heidelberg, 2003).

50. Ge, M. et al. Ensemble machine-learning-based analysis for in situ electron diffraction. *Adv. Theor. Simul.* **5**, 2100337 (2022).

51. Prins, R. Hydrogen spillover. Facts and fiction. *Chem. Rev.* **112**, 2714–2738 (2012).

52. Pan, Y. et al. Alloying effects on iron oxide redox pathways: insights into sustainable hydrogen-based reduction. *J. Phys. Chem. Lett.* **16**, 5506–5514 (2025).

53. Chinnasamy, C. N. et al. Mixed spinel structure in nanocrystalline $NiFe_2O_4$. *Phys. Rev. B* **63**, 184108 (2001).

54. Ge, M., Pan, Y., Liu, X., Zhao, Z. & Su, D. Automatic center identification of electron diffraction with multi-scale transformer networks. *Ultramicroscopy* **259**, 113926 (2024).

55. Perdew, J. P., Burke, K. & Ernzerhof, M. Generalized gradient approximation made simple. *Phys. Rev. Lett.* **77**, 3865–3868 (1996).

56. Perdew, J. P., Burke, K. & Ernzerhof, M. Perdew, Burke, and Ernzerhof Reply. *Phys. Rev. Lett.* **80**, 891–891 (1998).

57. Anisimov, V. I., Zaanen, J. & Andersen, O. K. Band theory and Mott insulators: Hubbard U instead of Stoner I. *Phys. Rev. B* **44**, 943–954 (1991).

58. Yu, X., Huo, C.-F., Li, Y.-W., Wang, J. & Jiao, H. Fe_3O_4 surface electronic structures and stability from GGA+U. *Surf. Sci.* **606**, 872–879 (2012).

59. Floris, A., de Gironcoli, S., Gross, E. K. U. & Cococcioni, M. Vibrational properties of MnO and NiO from DFT + U-based density functional perturbation theory. *Phys. Rev. B* **84**, 161102 (2011).

60. Meng, Y. et al. DFT study on H_2 and H adsorption and the electronic properties of single atom Cu modified Fe (111) surface. *Appl. Surf. Sci.* **505**, 144526 (2020).

61. Yang, T. et al. Structure and energetics of hydrogen adsorption on Fe_3O_4(111). *J. Mol. Catal. A: Chem.* **302**, 129–136 (2009).

62. Lennie, A. R. et al. Structures of Fe_3O_4 (111) surfaces observed by scanning tunneling microscopy. *Phys. Rev. B* **53**, 10244–10253 (1996).

63. Zhu, L., Yao, K. L. & Liu, Z. L. First-principles study of the polar (111) surface of Fe_3O_4. *Phys. Rev. B* **74**, 035409 (2006).

64. Whittaker, T. et al. H_2 oxidation over supported Au nanoparticle catalysts: evidence for heterolytic H_2 activation at the metal–support interface. *J. Am. Chem. Soc.* **140**, 16469–16487 (2018).

65. Henkelman, G., Uberuaga, B. P. & Jónsson, H. A climbing image nudged elastic band method for finding saddle points and minimum energy paths. *J. Chem. Phys.* **113**, 9901–9904 (2000).

66. Huang, S.-D., Shang, C., Zhang, X.-J. & Liu, Z.-P. Material discovery by combining stochastic surface walking global optimization with a neural network. *Chem. Sci.* **8**, 6327–6337 (2017).

Acknowledgements

Author contributions

Y.P. and D.S. designed the project. Y.P., X.L., and D.Z. performed the operando experiments. J.Z. helped with the sample preparation. Y.P., X.L., M.G., D.Z., and D.S. carried out the data analysis. S.Z. and L.Z. performed the theoretical calculations. Y.P., S.Z., L.Z., L.G., and D.S. co-wrote the paper. D.S. supervised the project. All authors discussed the results and contributed to the paper.

Competing interests

The authors declare no competing interests.

Additional information

Supplementary information The online version contains supplementary material available at https://doi.org/10.1038/s41467-025-63646-1.

Correspondence and requests for materials should be addressed to Dan Zhou, Liang Zhang or Dong Su.

Peer review information *Nature Communications* thanks Divakar Aireddy, and the other, anonymous, reviewer(s) for their contribution to the peer review of this work. A peer review file is available.

Reprints and permissions information is available at http://www.nature.com/reprints

Publisher's note Springer Nature remains neutral with regard to jurisdictional claims in published maps and institutional affiliations.